



This article appeared in a journal published by Elsevier. The attached copy is furnished to the author for internal non-commercial research and education use, including for instruction at the authors institution and sharing with colleagues.

Other uses, including reproduction and distribution, or selling or licensing copies, or posting to personal, institutional or third party websites are prohibited.

In most cases authors are permitted to post their version of the article (e.g. in Word or Tex form) to their personal website or institutional repository. Authors requiring further information regarding Elsevier's archiving and manuscript policies are encouraged to visit:

<http://www.elsevier.com/copyright>



Contents lists available at SciVerse ScienceDirect

Journal of the Mechanics and Physics of Solids

journal homepage: www.elsevier.com/locate/jmps

A phase field model incorporating strain gradient viscoplasticity: Application to rafting in Ni-base superalloys

M. Cottura^a, Y. Le Bouar^{a,*}, A. Finel^a, B. Appolaire^a, K. Ammar^b, S. Forest^b

^a Laboratoire d'Etude des Microstructures, CNRS/Onera, BP72, 92322 Châtillon Cedex, France

^b Mines ParisTech, Centre des Matériaux/CNRS UMR 7633, BP87, 91003 Evry Cedex, France

ARTICLE INFO

Article history:

Received 8 November 2011

Received in revised form

6 April 2012

Accepted 10 April 2012

Available online 16 April 2012

Keywords:

Phase transformation

Size effect

Phase field modeling

Strain gradient plasticity

Superalloys

ABSTRACT

The first formulation of a phase field model accounting for size-dependent viscoplasticity is developed to study materials in which microstructure evolution and viscoplastic behavior are strongly coupled. Plasticity is introduced using a continuum strain gradient formalism which captures the size effect of the viscoplastic behavior. First, the influence of this size effect on the mechanical behavior of the material is discussed in static microstructures. Then, the dynamic coupling between microstructure evolution and viscoplastic activity is addressed and illustrated by the rafting of the microstructure observed in Ni-base superalloys under creep conditions. It is found that the plastic size effect has only a moderate impact on the shape of the rafts but is crucial to reproduce the macroscopic mechanical behavior of that particular material.

© 2012 Elsevier Ltd. All rights reserved.

1. Introduction

Phase transformations play a major role for designing new materials with new properties, for improving the performance of existing materials, or defining new processes. It is indeed possible to combine the properties of different coexisting phases in an optimal way thanks to particular morphologies, which introduce internal scales besides the scale of interfaces. The phase distribution and morphology may be quite complex because they often result from complex evolutions controlled by the interaction between different phenomena: e.g. chemical diffusion, interfacial energies, mechanics (elasticity, plasticity, etc.) or electromagnetism. In the solid state, the mechanical behavior of the phases, from elasticity to elasto-viscoplasticity, has a major influence on the microstructure evolution. Indeed, phase transformations most often generate internal stresses coming from eigenstrains associated with changes in crystalline structure and in chemical composition. In the case of coherent precipitation (in the absence of plasticity) these stresses induce very anisotropic long-range interactions between precipitates at the origin of complex patterns (Khachaturyan, 1983). However, in many industrial materials, plasticity is likely to partially relax stresses when those reach the yield stress. This indeed may happen in three cases: (i) First, internal stresses can reach significant magnitudes as in bainites or martensites in steels where plasticity is responsible for the change in their morphologies (Li et al., 1998). (ii) Second, yield stresses are generally small at high temperature where diffusive phase transformations generally proceed. Hence, even rather small eigenstresses may be relaxed as during the late stage of γ' precipitation in superalloys (Yang et al., 2007). (iii) Finally, in service, materials are often submitted to external loadings and temperature changes. In that case, the microstructure evolution and the plastic activity are also obviously coupled.

* Corresponding author. Tel.: +33 1 46 73 45 92.

E-mail address: yann.lebouar@onera.fr (Y. Le Bouar).

Despite some early attempts (Ganghoffer et al., 1994; Wen et al., 1996; Ganghoffer et al., 1997; Su et al., 2006) the coupling of plastic relaxation with phase transformations has not been extensively investigated so far from a modeling point of view, because this requires efficient methods to handle microstructure evolution.

These last two decades, the phase field method (PFM) has emerged as the most powerful method for such a task, especially when stresses are involved in solids. Indeed, this method has been able (i) to explain the formation of complex microstructures, such as cuboidal microstructures in Ni-base superalloys (Wang et al., 1998; Boisse et al., 2007; Boussinot et al., 2009), twin structures in martensites (Wang et al., 2004; Finel et al., 2010), chessboard structures (Le Bouar et al., 1998) or hydrides precipitation in zirconium (Thuinet and Legris, 2010) and (ii) to capture subtle kinetic processes such as the slow down of coarsening in the presence of high elastic inhomogeneity (Onuki and Nishimori, 1991) or transitions between growth modes in ternary alloys involving slow and fast diffusing species (Viardin, 2010). So, it appears natural to include plasticity into a PFM to investigate its role in phase transformations.

Because plasticity in crystals is mainly due to the movement of dislocations, several works have explicitly introduced mobile dislocations in a PFM (Rodney, 2001; Wang et al., 2001; Koslowski et al., 2002) using an analogy between a dislocation loop and a thin precipitate. Dislocations are described with continuous fields for each slip system. The main advantage of this framework is that the elastic interactions between dislocations and/or precipitates are automatically accounted for. But it has two major flaws (i) first, the dislocations cores spread over several grid spacings: consequently realistic short-range interactions between dislocations require either subnanometer grid spacings, or a discrete description as in Rodney et al. (2003). (ii) Second, mechanisms other than dislocations glides (e.g. climb and cross slips at high temperatures, or twinning in materials with low stacking faults energy) are not accounted for currently.

To circumvent these drawbacks, plasticity can be introduced into PFMs through plastic strain field defined at mesoscale, supplied by internal variables such as hardening variables. As usual in continuum mechanics, evolution equations in the form of ordinary differential equations are postulated to describe plastic flow and hardening with parameters identified from experimental data. This approach has the advantage to phenomenologically include all the physical processes at the origin of plasticity. Works along this route have been only very recently proposed by several groups using mesoscale plasticity models differing by their descriptions of hardening, viscosity and plastic anisotropy.

The first attempts to couple a diffuse interface model with an isotropic plasticity model have been proposed in 2005. In Guo and Shi (2005), a PFM has been coupled to an isotropic plasticity model to study stress fields around defects such as holes and cracks. In Ubachs et al. (2005), a general formalism incorporating phase field and isotropic viscoplasticity with non-linear hardening has been proposed to investigate tin–lead solder joints undergoing thermal cycling. Since these pioneering works, similar approaches including isotropic plasticity models have been developed to study crystal growth (Uehara et al., 2007), martensites (Yamanaka et al., 2008), superalloys (Gaubert et al., 2008) and kinetics issues in diffusion controlled growth (Ammar et al., 2009, 2011). Finally, in the context of rafting in Ni-base superalloys, a few works have extended PFM with anisotropic plasticity model, either in a perfectly plastic model (Zhou et al., 2010), or in a crystal plasticity framework including both hardening and viscosity (Gaubert et al., 2010). It is worth mentioning that in Zhou et al. (2010), the yield stress as well as any hardening effects are not included.

Despite significant successes achieved by these models, they miss an important feature of the plastic behavior: the so-called *size effect*, also known as the Hall–Petch effect in polycrystals (Hall, 1951): the smaller the domains involved by plasticity, the harder the material. This size effect becomes significant when sizes involved are below a few microns, which is typically the case in an evolving microstructure.

The aim of the present work is precisely to demonstrate how a phase field method can be coupled to a mesoscale viscoplastic model accounting for the size effect of the plastic behavior within a framework similar to the one previously proposed by Gaubert et al. (2010). This size effect can only emerge from a viscoplastic model in which an intrinsic length is included and therefore, the viscoplastic model has to be chosen within the framework of the mechanics of generalized continua (Anand et al., 2010; Forest and Sievert, 2003).

The paper is divided as follows: In a first part, the phase field method and the viscoplastic model are presented, as well as their coupling within a coherent thermodynamic framework. In a second part, the predictions of the coupled model are analyzed. We first analyze static microstructures and we explain how the size effect modifies plastic activity and the resulting macroscopic mechanical behavior. Finally, the dynamic coupling between microstructure evolution and viscoplastic activity is addressed and illustrated by the rafting of the microstructure observed in Ni-base superalloys under creep conditions.

2. Model description

2.1. Phase field model

The coupling between phase field method and mesoscale viscoplastic model is presented in the context of the microstructural evolution in Ni-base superalloys. In these alloys, the disordered γ phase and the ordered γ' phase coexist at equilibrium. Following Boussinot et al. (2010), the superalloy is modeled as an effective binary alloy. In that case, in addition to the local concentration field $c(\mathbf{r}, t)$, three non-conservative structural fields $\eta_{i=1,3}(\mathbf{r}, t)$ are introduced to account for the degeneracy of the low temperature γ' phase. The four translational variants of γ' are described by the following long-range order parameters: $\{\eta_1, \eta_2, \eta_3\} = \eta_0\{1, 1, 1\}$, $\eta_0\{\bar{1}, \bar{1}, 1\}$, $\eta_0\{\bar{1}, 1, \bar{1}\}$, $\eta_0\{1, \bar{1}, \bar{1}\}$.

The main ingredient of phase field modeling is a mesoscopic free energy functional F relating the concentration and order parameters to the total free energy. It is usually decomposed into several contributions: bulk free energy, interface energies and elastic energy F_{el} , detailed in the next subsections. As usually done in mesoscale viscoplastic model, the free energy functional may also contain a viscoplastic contribution F_{vp} . Hence,

$$F = F_{ch}(c, \{\eta_i\}) + F_{el}(c, \{\eta_i\}, \boldsymbol{\varepsilon}^{el}) + F_{vp}(\boldsymbol{\alpha}, p) \quad (1)$$

where $\boldsymbol{\varepsilon}^{el}$ is the elastic strain tensor and F_{ch} the chemical free energy described in Section 2.1.1. The viscoplastic contribution F_{vp} , as well as the new fields necessary to describe hardening ($\boldsymbol{\alpha}, p$) will be introduced in Section 2.2.

2.1.1. Ginzburg–Landau free energy

The chemical free energy accounts for the volume free energy associated with phase transformation and interface energies. This free energy is given by a standard Ginzburg–Landau functional:

$$F_{ch}(c, \{\eta_i\}) = \int_V f_{hom}(c, \{\eta_i\}) + \frac{\lambda}{2} |\nabla c|^2 + \frac{\beta}{2} \sum_i |\nabla \eta_i|^2 dV \quad (2)$$

where V is the volume, λ and β are gradient energy coefficients and $f_{hom}(c, \{\eta_i\})$ is the free energy density of a homogeneous system characterized by the concentration c and order parameters η_i . As usual, $f_{hom}(c, \{\eta_i\})$ is approximated by a Landau polynomial expansion with respect to the order parameters. Its form is dictated by the symmetry loss during the $\gamma \rightarrow \gamma'$ phase transformation. Following Boussinot et al. (2010), the lowest possible order of the expansion has been chosen:

$$f_{hom}(c, \{\eta_i\}) = \Delta f \left[\frac{1}{2} (c - c_\gamma)^2 + \frac{B}{6} (c_2 - c) \sum_{i=1,3} \eta_i^2 - \frac{C}{3} \eta_1 \eta_2 \eta_3 + \frac{D}{12} \sum_{i=1,3} \eta_i^4 \right] \quad (3)$$

where Δf is an energy density scale and c_2 an arbitrary concentration chosen between the equilibrium concentrations c_γ and $c_{\gamma'}$ of the coexisting phases. B , C and D are constants related to c_2 , c_γ , $c_{\gamma'}$ and to the equilibrium long-range order parameter η_0 . In all the subsequent calculations, we have used the equilibrium concentrations $c_\gamma = 0.15$ and $c_{\gamma'} = 0.231$, as well as $c_2 = 0.18$. Following Boussinot et al. (2010), forcing η_0 to saturate at 1 gives $B = 0.162$, $C = 0.01458$ and $D = 0.022842$ and the non-dimensional coefficients: $\tilde{\lambda} = \lambda / (\Delta f d^2)$ and $\tilde{\beta} = \beta / (\Delta f d^2)$, where d is the grid spacing, are chosen to be $\tilde{\lambda} = 0.21$ and $\tilde{\beta} = 9.75 \times 10^{-4}$.

2.1.2. Elastic energy

The potential elastic energy in the framework of linear elasticity reads:

$$F_{el}(\boldsymbol{\varepsilon}^{el}) = F_{el}^a(\bar{\boldsymbol{\varepsilon}}) + \frac{1}{2} \int_V \boldsymbol{\lambda} : \boldsymbol{\varepsilon}^{el} : \boldsymbol{\varepsilon}^{el} dV \quad (4)$$

where $\boldsymbol{\lambda}$ stands for the local elastic moduli tensor and $\bar{\boldsymbol{\varepsilon}}$ for the average strain. $F_{el}^a(\bar{\boldsymbol{\varepsilon}})$ is a homogeneous term which depends on the choice of the boundary conditions. In the case of a traction along [100] under a constant applied stress σ_{11}^a , $F_{el}^a = -V \sigma_{11}^a \bar{\varepsilon}_{11}$. In the case of an experiment controlled by strain, $F_{el}^a = 0$.

Assuming that the local concentration is the relevant field for discriminating the elastic properties, $\tilde{\boldsymbol{\lambda}}$ is chosen as a linear function of $c(\mathbf{r})$ and is thus space dependent (Boussinot et al., 2010).

Accounting for plasticity in the small strain framework, the total strain $\boldsymbol{\varepsilon}(\mathbf{r})$ can be divided into three contributions:

$$\boldsymbol{\varepsilon}(\mathbf{r}) = \boldsymbol{\varepsilon}^{el}(\mathbf{r}) + \boldsymbol{\varepsilon}^0(\mathbf{r}) + \boldsymbol{\varepsilon}^p(\mathbf{r}) \quad (5)$$

where $\boldsymbol{\varepsilon}^p(\mathbf{r})$ is the plastic strain tensor with time evolution detailed in Section 2.2. $\boldsymbol{\varepsilon}^0(\mathbf{r})$ is the stress-free strain tensor associated with the lattice parameter change during the $\gamma \rightarrow \gamma'$ transformation. Assuming Vegard's law:

$$\boldsymbol{\varepsilon}^0(\mathbf{r}) = \varepsilon^T \Delta c(\mathbf{r}) \mathbf{1} \quad (6)$$

where $\mathbf{1}$ is the identity matrix and $\varepsilon^T = \delta / (c_{\gamma'} - c_\gamma)$. The misfit is related to the lattice parameters a_γ and $a_{\gamma'}$ of the stress-free γ and γ' phases $\delta = 2(a_{\gamma'} - a_\gamma) / (a_{\gamma'} + a_\gamma)$.

In the case of diffusion controlled phase transformations, static mechanical equilibrium can be assumed since relaxation of the elastic waves is by orders of magnitude faster than the evolution of concentration, order parameters, and plastic strain governed by viscoplasticity. Therefore, at any time, elastic strain can be computed by solving mechanical equilibrium assuming stress-free strain and constant plastic strain. This can be done by minimizing the potential elastic energy with respect to displacements accounting for given boundary conditions. When the elastic constants of the coexisting phases differ, mechanical equilibrium has to be solved iteratively as in Boussinot et al. (2010).

2.1.3. Kinetic equations for the chemical fields

The time evolution of the concentration and order parameters is governed by kinetic equations relating time derivatives to the corresponding driving forces, defined as the functional derivatives (noted $\delta F / \delta \cdot$) of F with respect to the fields. Assuming linear constitutive relationships, the Cahn–Hilliard equation is recovered for the conserved concentration field

and the Allen–Cahn equation for the non-conserved order parameter ones:

$$\frac{\partial c}{\partial t}(\mathbf{r}, t) = M \nabla^2 \frac{\delta F}{\delta c(\mathbf{r}, t)} \quad (7)$$

$$\frac{\partial \eta_i}{\partial t}(\mathbf{r}, t) = -L \frac{\delta F}{\delta \eta_i(\mathbf{r}, t)} \quad (8)$$

The kinetic coefficients M and L , related to diffusion and structural relaxation, respectively, are assumed constant. Following Gaubert et al. (2010), M is such as to recover the interdiffusion coefficient $D = D_0 \exp(-\Delta U/k_B T)$ with $D_0 = 1.45 \times 10^{-4} \text{ m}^2 \text{ s}^{-1}$ and $\Delta U = 2.8 \text{ eV}$ (Fujiwara et al., 1999). We have used $L = 100 M d^{-2}$, where d is the grid spacing, to ensure that kinetics is much faster for the order parameter than for the concentration field.

2.2. Strain gradient mesoscale plasticity model

The mesoscale viscoplastic model coupled to the phase field method is presented in this section. As explained in the introduction, the key point is that the size effect due to the plastic behavior has to be taken into account. Within the framework of continuum mechanics, this size effect can only emerge from a plastic model in which an intrinsic length is included.

Size-dependent constitutive models can be obtained by resorting to the mechanics of generalized continua, like second gradient and micromorphic theories (Mindlin and Eshel, 1968; Eringen and Suhubi, 1964). Isotropic strain gradient plasticity models have been developed since the early 1980s to account for size effect and deformation patterning observed in metals (Aifantis, 1987). Second, size-dependent crystal plasticity models have been proposed by Fleck and Hutchinson (1997) using second gradient and Cosserat (Forest et al., 1997) theories. More recently the microforce approach put forward by Gurtin was applied to crystal plasticity as an alternative (Gurtin, 2002; Svendsen, 2002). The curl of the plastic strain tensor or, equivalently, the lattice curvature tensor (gradient of the deformation induced lattice rotation) are directly related to the notion of geometrically necessary dislocations well-known in physical metallurgy (Ashby, 1971; Steinmann, 1996). Constitutive equations involving functions of the plastic strain gradient or, equivalently, of the densities of geometrically necessary dislocations introduce internal length scales that are responsible for a size effect in the resulting behavior. In the present work, we have chosen to use a strain gradient viscoplastic model similar to the one proposed in Aifantis (1987) and Forest and Aifantis (2010) which has the advantage of simplicity and in which the intrinsic plastic length is easily controlled through the value of a single parameter. The framework used below will be similar to the one developed in Gaubert et al. (2010) but with the addition of a heterogeneous component in the viscoplastic free energy density. Also, for the sake of simplicity, the present formulation is limited to isotropic viscoplasticity even though the extension to an anisotropic viscoplastic behavior could be obtained by explicitly introducing an appropriate set of slip systems. The derivation of the simple isotropic model within a coherent thermodynamic framework is presented in this section.

The plastic state of the material is described classically with two internal variables $\tilde{\alpha}$ and p related to kinematic and isotropic hardening, respectively (Lemaitre and Chaboche, 1990). They enter the free energy as follow:

$$F_{vp}(\tilde{\alpha}, p) = \int_V \frac{1}{3} C \tilde{\alpha} : \tilde{\alpha} + \frac{1}{2} H p^2 + \frac{1}{2} A |\nabla p|^2 dV \quad (9)$$

A simple quadratic form is assumed for the contribution of $\tilde{\alpha}$. The contribution of p has also a quadratic part describing linear isotropic hardening, which can be easily extended to the case of a non-linear isotropic hardening (Lemaitre and Chaboche, 1990). The last term in (9), proportional to the square gradient of p introduces an intrinsic length scale in the plastic model. A dimension analysis shows that this intrinsic length is proportional to the square root of the gradient coefficient A .

The evolution of the material leads to an energy dissipation. The local intrinsic dissipation is given by

$$\phi = \tilde{\sigma} : \tilde{\dot{\epsilon}}^p - \mathbf{X} : \tilde{\dot{\alpha}} - R \dot{p} \quad (10)$$

where the thermodynamic forces associated with the internal variables are given by

$$\mathbf{X} = \frac{\delta F}{\delta \tilde{\alpha}} = \frac{2}{3} C \tilde{\alpha} \quad (11)$$

$$R = \frac{\delta F}{\delta p} = H p - A \Delta p \quad (12)$$

These thermodynamic forces correspond to the hardening variables defining the elastic domain and the corresponding plastic/viscoplastic potential (Lemaitre and Chaboche, 1990). More precisely, \mathbf{X} is the back-stress, i.e. the center of the elastic domain, and R is its radius. In this formulation, we assume that all strain gradient effects are attributed to the free energy (9), following Gurtin and Anand (2009) and Forest and Aifantis (2010). More general models could also incorporate some dissipative contributions associated with strain gradients.

The kinetic equations of the viscoplastic model are obtained within a thermodynamic framework by postulating the existence of a convex dissipation potential Ω which depends on stress $\tilde{\sigma}$ and on the thermodynamic forces in the following way (Lemaitre and Chaboche, 1990):

$$\Omega(\tilde{\sigma}, \tilde{\mathbf{X}}, R) = \int_V \tilde{\Omega} \left(J_2(\tilde{\sigma} - \tilde{\mathbf{X}}) - (R_0 + R) + \left[\frac{D}{2C} J_2^2(\tilde{\mathbf{X}}) - \frac{2DC}{9} J_2^2(\tilde{\alpha}) \right] \right) dV \quad (13)$$

where R_0 , C and D are coefficients which may depend on temperature. J_2 defining a distance in stress space is given by $J_2(\tilde{\sigma}) = \sqrt{\frac{3}{2}(\tilde{\sigma}' : \tilde{\sigma}')}$ where $\tilde{\sigma}' = \tilde{\sigma} - \frac{1}{3} \text{Tr}(\tilde{\sigma}) \mathbf{1}$ is the deviatoric stress.

The normal dissipative laws are then expressed as

$$\dot{p} = -\frac{\delta \Omega}{\delta R} = -\frac{\partial \tilde{\Omega}}{\partial R} \quad (14)$$

$$\dot{\tilde{\mathbf{e}}}^p = \frac{\delta \Omega}{\delta \tilde{\sigma}} = \frac{3}{2} \dot{p} \frac{\tilde{\sigma}' - \tilde{\mathbf{X}}'}{J_2(\tilde{\sigma} - \tilde{\mathbf{X}})} \quad (15)$$

$$\dot{\tilde{\alpha}} = -\frac{\delta \Omega}{\delta \tilde{\mathbf{X}}} = \dot{\tilde{\mathbf{e}}}^p - D \tilde{\alpha} \dot{p} \quad (16)$$

Combining these expressions, it is found that p is the cumulative plastic strain since $\dot{p} = \sqrt{\frac{2}{3} \dot{\tilde{\mathbf{e}}}^p : \dot{\tilde{\mathbf{e}}}^p}$. Finally, the following dissipation potential density has been assumed:

$$\tilde{\Omega}(f) = \frac{K}{N+1} \left\langle \frac{f}{K} \right\rangle^{N+1} \quad (17)$$

where $\langle a \rangle$ stands for the positive part of a and N, K are positive parameters. This choice leads to a Norton type flow rule:

$$\dot{p} = \left\langle \frac{J_2(\tilde{\sigma} - \tilde{\mathbf{X}}) - R_0 - R}{K} \right\rangle^N \quad (18)$$

where R_0 appears now to be the initial yield stress and R the isotropic hardening. It is worth noting that R includes both linear isotropic hardening and the strengthening resulting from the plastic size effect (12).

In heterogeneous materials, the viscoplastic parameters C, D, H, A, N, K and R_0 depend on position \mathbf{r} . In the particular case of γ/γ' superalloys under creep loading, only γ undergoes plastic strain while γ' behaves elastically. To reproduce this behavior all the viscoplastic parameters have been set at their value in the γ phase, except the initial yield stress R_0 which is interpolated between R_0^γ and $R_0^{\gamma'}$ as follows:

$$R_0(\mathbf{r}) = \bar{R}_0 + R'_0 \tanh \left[\theta \left(\frac{1}{3\eta_0^2} \sum_{i=1,3} \eta_i^2(\mathbf{r}) - \frac{1}{2} \right) \right] \quad (19)$$

with $\bar{R}_0 = (R_0^\gamma + R_0^{\gamma'})/2$, $R'_0 = (R_0^{\gamma'} - R_0^\gamma)/2$ and θ a parameter controlling plasticity in the interface.

In all the calculations, we have used $\theta = 100$ which leads to variations of the parameters over a grid spacing d , a distance smaller than the interface width. Other values have been tested to check that the influence on the microstructural evolution is negligible. Moreover, for purely numerical reasons, the value of $R_0^{\gamma'}$ is chosen large enough (100 GPa) to prevent any plastification of γ' even in presence of a characteristic plastic length.

3. Results

3.1. Plasticity in a static microstructure

3.1.1. 1D: Analytical solution

At first, we have investigated the viscoplastic model in a simple static microstructure so as to make a clear link between its parameters and a characteristic plastic length.

For that purpose, a 1D configuration has been chosen which mimics a periodic arrangement of elastic γ' layers with thickness ℓ and plastic γ channels with thickness s along the x direction (Fig. 1). This two phases laminate is submitted to a tensile strain along x . This configuration was also analyzed by Cordero et al. (2010) in the context of single crystal strain

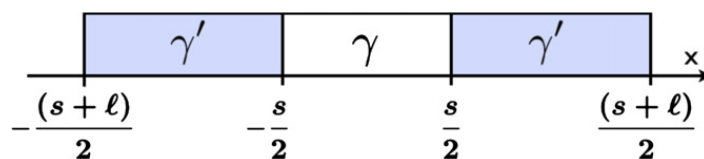


Fig. 1. Configuration used to derive the analytical solution.

gradient plasticity under shear loading conditions. We have considered cubic homogeneous elasticity, isotropic hardening and no kinematic hardening. Moreover, the misfit between γ and γ' has been neglected.

In the limit of time independent plasticity ($\dot{\epsilon}_{11} \rightarrow 0$), an analytical solution for the cumulative plastic strain p can be found along the following lines (see Appendix for details). First the J_2 yield surface is expressed for the specific 1D geometry considered here: $J_2(\boldsymbol{\sigma}) = |\sigma_{11} - \sigma_{22}(x)|$, where σ_{11} is homogeneous to fulfill mechanical equilibrium. Using von Mises criterion in γ , we have

$$R_0 + Hp(x) - A\Delta p(x) = |\sigma_{11} - \sigma_{22}(x)| \quad (20)$$

Using Hooke's law $\sigma_{22}(x)$ can be written in terms of σ_{11} and p and replaced in Eq. (20) to give a second order differential equation. Integrating this equation with the boundary conditions leads to

$$p(x) \propto 1 - \frac{\cosh(\omega x)}{\cosh(\omega s/2)} \quad \text{with } \omega^2 = \frac{1}{A} \left(H + \frac{1}{2} \frac{E}{1-\nu} \right) \quad (21)$$

where E and ν are Young's modulus and Poisson's ratio in the x direction.

The characteristic plastic length $\xi = 1/\omega$ can be identified, which varies as \sqrt{A} as expected. ξ depends on the isotropic hardening modulus H and on Young's modulus E . In a simplified approach H and E can be linked to the slopes of plastic and elastic parts of the σ vs. ϵ curve, respectively. Provided that H is much smaller than E , a good estimate of the plastic length is $\xi = \sqrt{A/E}$.

Typical profiles of p are shown in Fig. 2 for different values of ξ at the same average strain $\bar{\epsilon}_{11} = 5 \times 10^{-3}$, using parameters in Table 1 and $H = 4.3$ GPa. Analytical solutions obtained with Eq. (21) are plotted with continuous lines. Plastic deformation is of course confined in the γ channel. Its gradients are located at the γ/γ' interfaces and extend over ξ . When $\xi \ll s$, p is homogeneous in almost the whole γ channel, and tends to the value given by conventional plasticity ($\xi \rightarrow 0$). The homogeneous region of the plastic strain starts to disappear when ξ is about 15% of channel thickness. For $\xi \approx s/3$, p exhibits an almost parabolic profile with a significant decrease in the maximum cumulative plastic strain at $x=0$. As a consequence, the elastic strain as well as σ_{11} become higher as ξ increases for a given $\bar{\epsilon}_{11}$. It must be noted that for the γ' volume fraction $\tau_{\gamma'} = 0.7$ used in Fig. 2, the influence of ξ on σ_{11} remains moderate (for $\xi = 0.1$ nm, $\sigma_{11} = 292$ MPa; for $\xi = 38$ nm, $\sigma_{11} = 350$ MPa).

In Fig. 2, the corresponding numerical calculations are plotted with symbols. The kinetic coefficients M and L in Eqs. (7) and (8) are set to zero to freeze the microstructure. $\bar{\epsilon}_{11}$ has been applied at a very small rate $\dot{\bar{\epsilon}}_{11} = 10^{-10} \text{ s}^{-1}$ in order to match the conditions used to derive the analytical solution. A perfect match between the analytical solution and numerical simulation is found, which validates the numerical implementation of our model.

3.1.2. Global mechanical behavior

Aiming at investigating microstructure evolutions coupled to viscoplasticity in Ni-base superalloys, the first step is to properly assess the size effect as predicted by the viscoplastic model on the mechanical behavior of a static real

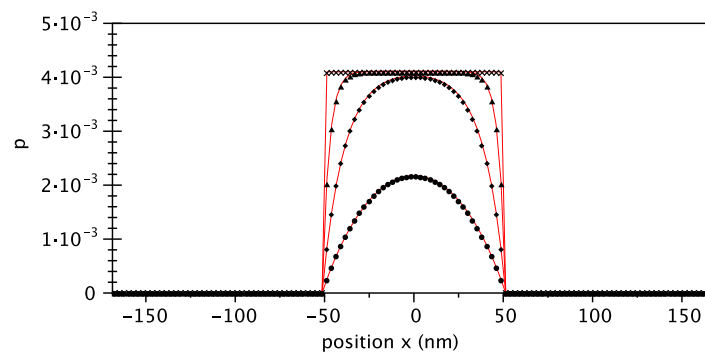


Fig. 2. Profiles of cumulative plastic strain for different values of ξ at $\bar{\epsilon}_{11} = 5 \times 10^{-3}$ in a 1D configuration of two phases: γ channel (plastic) of thickness $s = 102$ nm and γ' precipitates (elastic) of thickness $\ell = 235$ nm. The red curves are the analytical solutions corresponding to the simulations with (x) $\xi = 0.1$ nm, (\blacktriangle) $\xi = 3.8$ nm, (\blacklozenge) $\xi = 12$ nm, (\bullet) $\xi = 38$ nm. (For interpretation of the references to color in this figure caption, the reader is referred to the web version of this article.)

Table 1

Elastic moduli (Gaubert et al., 2010) and viscoplastic parameters at $T = 950$ °C. The parameters of γ have been identified from macroscopic experiments (Espíe, 1996; Gaubert, 2009).

Phase	C_{11} (GPa)	C_{12} (GPa)	C_{44} (GPa)	C (GPa)	D	N	K (MPa s ^{1/N})	R_0 (MPa)
γ	197	144	90	150	1900	5	150	86
γ'	193	131	97	150	1900	5	150	10 ⁵

microstructure. For that purpose, we have studied an AM1-type superalloy under loading for which data concerning its mechanical behavior are available in the literature. More specifically, we have used tensile curves σ vs. ε obtained with a tensile strain rate $\dot{\varepsilon}_{11} = 10^{-3} \text{ s}^{-1}$, in conditions where the microstructure is known not to evolve significantly.

The simulations have been performed considering a 3D periodic model configuration: a cube-shaped precipitate inside a cubic matrix. It mimics a periodic array of identical γ' precipitates aligned along the cubic orientations separated by narrow γ channels. To reproduce the features of realistic microstructures observed in AM1 (Diologent, 2002), such as the volume fraction $\tau_{\gamma'} = 0.7$ and the average precipitate size $\sim 450 \text{ nm}$, we have considered γ' precipitates 456 nm large and γ channels 56 nm wide. We used a discretization of 256^3 nodes and a node spacing of $d=2 \text{ nm}$. Moreover, the fields identifying the microstructure have been relaxed so as to obtain diffuse interfaces. All the model parameters have been selected from experimental measurements. According to Royer et al. (1998) and Diologent et al. (2003), the lattice mismatch is $\delta = -0.1\%$. The elastic moduli and the viscoplastic parameters have been taken from Gaubert et al. (2010) (Table 1). For AM1, it has been shown that isotropic hardening is small (Hanriot, 1993) and therefore we neglect the hardening modulus H in our simulations.

In Fig. 3, the curve σ vs. ε predicted with the parameters in Table 1 for the γ bulk phase is compared to the experimental tensile curve of Espié (1996), with $\dot{\varepsilon}_{11} = 9 \times 10^{-4} \text{ s}^{-1}$. As expected, an excellent agreement is achieved. Assuming a perfectly elastic behavior for γ' , and using the viscoplasticity parameters for γ without plastic length ($\tilde{\xi} = 0$), the calculations (dashed black) underestimate the mechanical behavior of the two-phase alloy as compared to experiments (blue +): at $\varepsilon = 0.07\%$, $\sigma \approx 480 \text{ MPa}$ is below the experimental value $\sigma \approx 560 \text{ MPa}$. This difference can be attributed to the confinement of plasticity in γ which strengthens the material. This demonstrates the necessity of including a plastic size effect to predict more quantitatively the flow stress curve of AM1 superalloys.

This strengthening is introduced in the viscoplastic model by tuning the additional parameter A . We have chosen $A = 5 \times 10^7 \text{ MPa nm}^2$ corresponding to $\tilde{\xi} = 26 \text{ nm}$, which is half the γ channel width. For such a value, a better agreement is achieved with the measurements as shown in Fig. 3. It is worth noting that increasing $\tilde{\xi}$ such that $\tilde{\xi} \gg s$ makes γ behave purely elastically: the mechanical behavior of the two-phase alloy becomes closer to a linear elastic behavior with a slope corresponding to the slope at the beginning of the tensile curves in Fig. 3. The present method could be used to identify $\tilde{\xi}$, provided that the elastic constants of the γ and γ' phases have been accurately obtained.

Finally, the softening effect, characterized by a decrease of the flow stress shortly after the beginning of yielding often observed in single crystal Ni-base superalloys, is not accounted for in our model (Levkovitch et al., 2006). However, in the service conditions studied in the present work (small deformation rate), this softening is hardly visible for the AM1 superalloy (Espié, 1996; Gaubert, 2009).

3.2. Microstructural evolution coupled to a viscoplastic activity

In this section, the rafting (directional coarsening) of γ' precipitates in AM1-type superalloy under creep loading is investigated with the coupled phase field method/viscoplastic model. In particular, the question of whether the size effect has an influence or not on the transformation kinetics and on the morphological evolution is addressed. It must be stressed that this alloy is particularly well suited for this purpose because plastic activity is only observed within the γ channels, at temperatures around $950\text{--}1050^\circ\text{C}$. We have proceeded in two steps: (i) first, a typical cuboidal microstructure is generated accounting for elasticity only, with no applied stress. (ii) Second, the evolution of this microstructure during the creep experiment is investigated. SEM images of the microstructure corresponding to these steps in AM1 superalloys can be observed in Fig. 4.

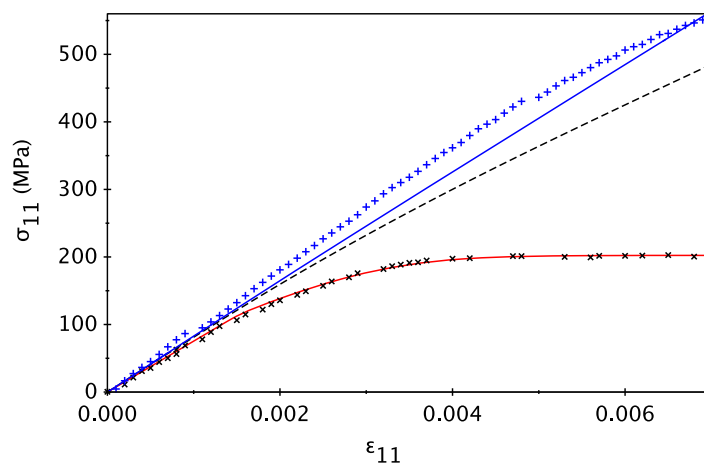


Fig. 3. Stress–strain curves at $T=950^\circ\text{C}$ of the bulk γ phase ($\dot{\varepsilon}_{11} = 9 \times 10^{-4} \text{ s}^{-1}$) and of the AM1 superalloy ($\dot{\varepsilon}_{11} = 10^{-3} \text{ s}^{-1}$). The tensile axis is parallel to the $[100]$ crystallographic direction. Experimental measurements are represented by \times symbols for pure γ and by blue $+$ symbols for AM1 (Espié, 1996; Gaubert, 2009). PFM results with lines in red for pure γ ; in dashed black ($\tilde{\xi} = 0$) or blue ($\tilde{\xi} = 26 \text{ nm}$) for AM1. (For interpretation of the references to color in this figure caption, the reader is referred to the web version of this article.)

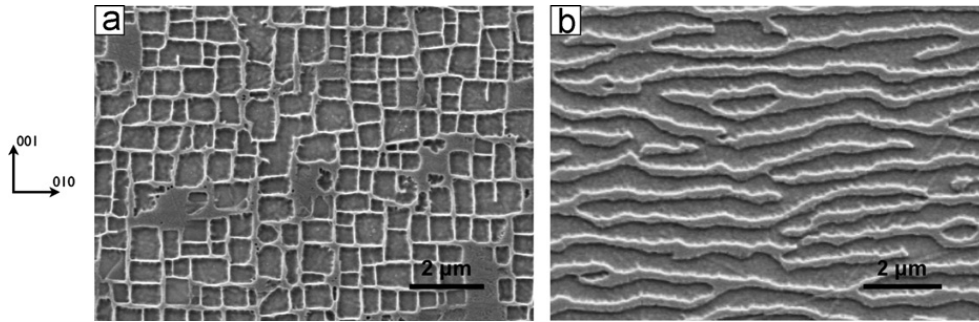


Fig. 4. SEM observations of AM1: (a) before aging (b) after a 72 h creep experiment under 150 MPa along the $[0\ 0\ 1]$ axis at $T = 1050\ ^\circ\text{C}$ (Gaubert, 2009).

3.2.1. Initial cuboidal microstructure and elastic parameters

The cuboidal microstructure is achieved using the PFM presented in Section 2. The only required input parameters are the interfacial energy ($\sigma_{\text{exp}} = 2\ \text{mJ/m}^2$), the misfit ($\delta = -0.1\%$) and the elastic constants. The choice of the elastic constants is detailed in the following paragraph.

As shown in Gaubert et al. (2010), if we use the γ/γ' elastic moduli available in the literature for the AM1 at $T=950\ ^\circ\text{C}$ (Table 1), the PFM predicts the formation of an anisotropic microstructure where the γ/γ' interfaces are aligned along the cubic directions. However, this microstructure contains many γ' precipitates of irregular shape which are rarely observed in AM1 (Fig. 4(a)). A systematic study in Hu and Chen (2001) has shown the importance of the inhomogeneity of the shear elastic constant $C' = (C_{11} - C_{12})/2$ on the microstructure formed. Microstructures made of well aligned cuboidal precipitates, as observed in AM1, can be generated only when the inhomogeneity of C' is large enough. This suggests that the difference of about 10% in C' between γ and γ' obtained in Gaubert et al. (2010) is underestimated. The inaccuracy of the measurements can be attributed to the inverse process used to infer the elastic constants of each phase from the behavior of the two-phase alloy (Fahrman et al., 1999; Sieborger et al., 2001). For that reason, we have increased the inhomogeneity of C' up to 40% while keeping the same elastic anisotropy $2C_{44}/(C_{11} - C_{12}) = 3.3$. This has been carried out by changing C'_{12} to 118 GPa and C'_{44} to 124 GPa, keeping all other moduli in Table 1 unchanged.

The initial cuboidal microstructure was generated in the elastic regime from an initial disordered γ phase with stress-free boundary conditions. The total size of the 2D system is $2.3 \times 2.3\ \mu\text{m}^2$ discretized with 512^2 nodes. The last stage of the formation process is shown in Fig. 5(0) where the gray corresponds to the γ matrix and the different colors are related to the four translational variants of the γ' phase. After 16 h at $950\ ^\circ\text{C}$, the microstructure consists of cuboidal precipitates, well aligned along the cubic directions, separated by well defined γ channels (Fig. 5(0)). The initial volume fraction of γ' precipitates is 0.63 and their average size is 319 nm. The γ channels have an average size of 78 nm. This microstructure is in good agreement with microstructures observed in AM1. Finally, it is worth mentioning that slight modifications of the C' inhomogeneity has significant consequences on the microstructure. The necessity of a large enough C' inhomogeneity could be used in the future as a new ingredient to improve the inverse process designed for the determination of the elastic constants of the γ and γ' phases.

3.2.2. Rafting under creep

In the second step, a constant stress $\sigma^a = 150\ \text{MPa}$ has been applied to the microstructure in Fig. 5(0) along the horizontal axis, while holding temperature at $950\ ^\circ\text{C}$. In order to test the influence of the plastic characteristic length on the microstructure evolution, three different creep simulations have been performed. First, a purely elastic case has been considered (Fig. 5(a)–(d)). Second, an elasto-viscoplastic one without size effect (Fig. 5(h)–(j)) was completed to make a full comparison with the last one where the plastic size effect are accounted for (Fig. 5(e)–(g)). As in Section 3.1.2, ξ is set to 26 nm. This value corresponds to one third of the initial average channel width.

For all evolutions in Fig. 5, the microstructure tends towards a morphology of rafts aligned along the same direction perpendicular to the tensile axis. This is in agreement with previous studies of creep along one cubic direction showing that the elastic and plastic driving forces lead to the same raft orientation (Boussinot et al., 2010; Zhou et al., 2008). Comparing the elastic and plastic cases clearly shows that viscoplasticity has two major impacts on the evolution. First, it influences the kinetics: the formation of the rafts is faster when plastic activity is accounted for. This behavior is clearly demonstrated by the splitting of the larger precipitate observed in the first and rows in Fig. 5. The splitting happens at $t=3.5\ \text{h}$ with viscoplasticity (Fig. 5(h)) and at $t=5.8\ \text{h}$ without viscoplasticity (Fig. 5(b)).

Second, at a stage where straight rafts are observed in the elastic case, the microstructure in the plastic simulation is still wavy. This feature is in agreement with a previous study using an anisotropic viscoplastic model (Gaubert et al., 2010). Furthermore, in the late stage of the viscoplastic simulation, the evolution becomes hardly noticeable and the microstructure is almost frozen (last column in Fig. 5), while in the elastic case it is still evolving to give flat rafts after $t=72.6\ \text{h}$ (Fig. 5(d)). Finally, it can be noted that the volume fraction of γ' decreases slightly with viscoplasticity: at $t=36.3\ \text{h}$, $\tau_{\gamma'} = 0.59$ in the elastic case whereas $\tau_{\gamma'} = 0.57$ and $\tau_{\gamma'} = 0.55$ in the viscoplastic cases with $\xi = 26\ \text{nm}$ and $\xi = 0$, respectively.

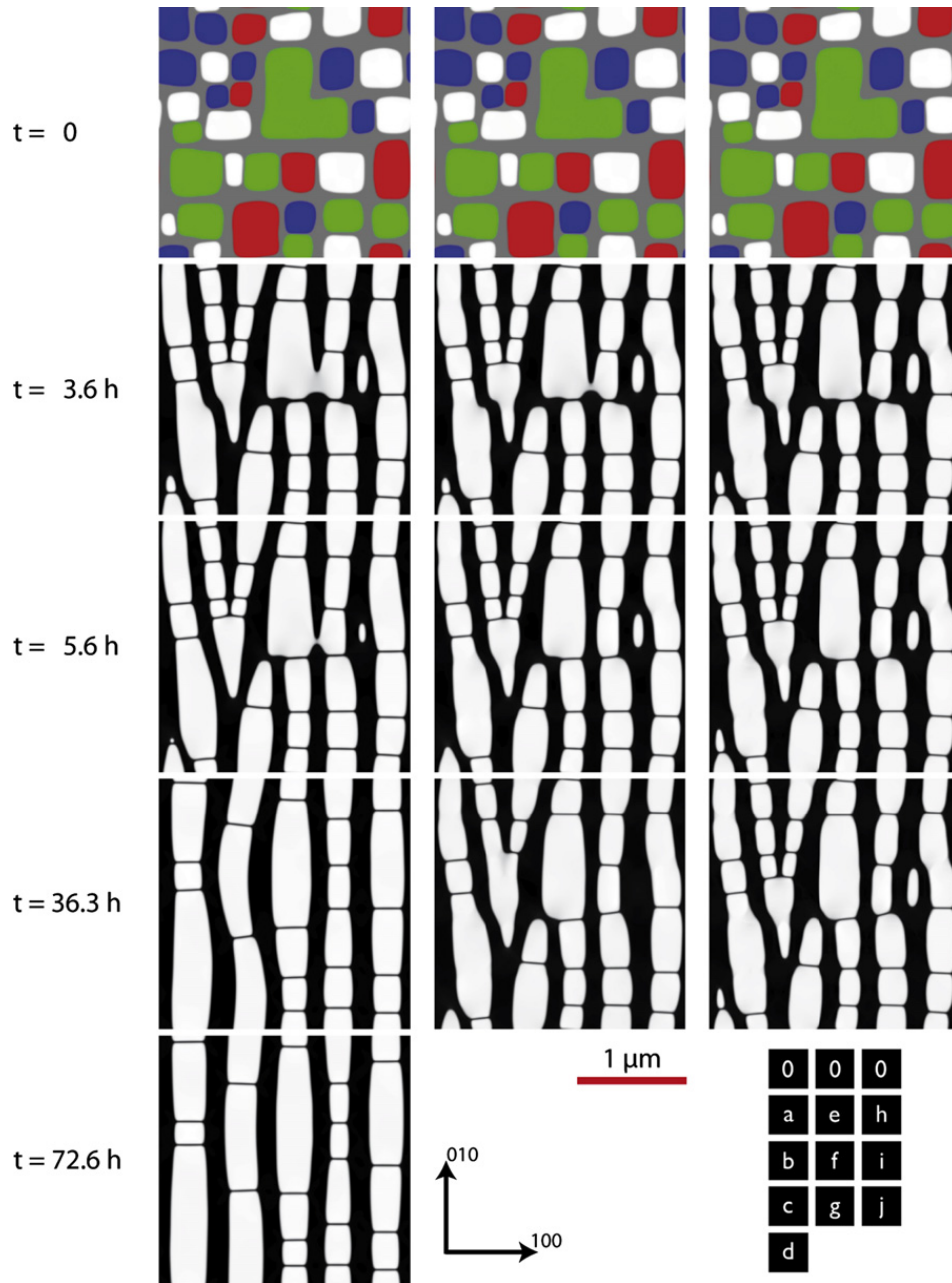


Fig. 5. Starting from the initial microstructure generated under stress-free conditions (0), microstructure evolutions under a constant tensile stress along the [100] axis (150 MPa) predicted by (a)–(d) the elastic PFM; (e)–(g) the elasto-viscoplastic PFM including size effect ($\tilde{\xi} = 26$ nm); (h)–(j) the elasto-viscoplastic PFM ($\tilde{\xi} = 0$). The shade of gray are in accordance with the value of the concentration field $c(\mathbf{r}, t)$; the white and black areas represent the γ' and γ phase, respectively. The nomenclature of the images is indicated in the lower right corner. (For interpretation of the references to color in this figure caption, the reader is referred to the web version of this article.)

3.2.3. Influence of the plastic length scale

The comparison between the middle and right columns shows the influence of the characteristic plastic length $\tilde{\xi}$. Again, the kinetics of rafting is estimated with the time necessary for the large precipitate to split into two smaller precipitates. When $\tilde{\xi} = 26$ nm, splitting occurs at a later time ($t = 4$ h) than when $\tilde{\xi} = 0$ ($t = 3.5$ h). Therefore, the plastic length slows down the raft formation and gives a kinetics closer to the elastic case. This behavior is expected because the plastic length leads to an increase in flow stress and therefore to a decrease of plastic activity. Furthermore, as already noted when $\tilde{\xi} = 0$, the microstructure evolution predicted with $\tilde{\xi} = 26$ nm is almost frozen after the formation of the rafts (Fig. 5(g)). The frozen configurations obtained in the two viscoplastic cases (Fig. 5(g) and (j)) are rather similar: the plastic length has moderate consequences on the morphological evolution at long time for the particular evolution considered. Still, a few differences are noticeable. Some small precipitates have dissolved when $\tilde{\xi} \neq 0$ but they can still be observed when $\tilde{\xi} = 0$. Moreover, as already mentioned, $\tau_{\gamma'}$ is slightly larger with plastic length than without, resulting in slightly smaller γ channels.

The difference between the two viscoplastic cases is more obvious when considering the plastic fields, e.g. the cumulated plastic strain p at $t=36.3$ h (first row in Fig. 6). As expected, plastic activity is confined in γ , mainly in the vertical channels in both cases. When $\tilde{\xi} = 0$, p is almost homogeneous in all the vertical γ channels (Fig. 6(b)). The plastic length introduces several differences with conventional viscoplasticity (Fig. 6(a) and (b)). (i) Plastic activity becomes weaker due to the increase in flow stress. (ii) The decrease of p is more pronounced in the thin channels than in the large ones (Fig. 6(a)). (iii) p varies more smoothly. These features are also clearly observed with the profile of p perpendicular to the rafts (Fig. 7). The variations of p along the profile are smoother and smaller when $\tilde{\xi} = 26$ nm (full red line) than when $\tilde{\xi} = 0$ (dashed line). Large channels are less sensitive to the plastic length than small ones: when $\tilde{\xi} = 0$, $p \approx 1.2 \times 10^{-3}$ in all the channels; when $\tilde{\xi} = 26$ nm, $p \approx 9.8 \times 10^{-4}$ in the center of channels 190 nm wide, and decreases to $p \approx 4.9 \times 10^{-4}$ in channels 75 nm wide. Finally, it can be noticed that small regions at the center of the vertical channels (Figs. 6(b) and 7) display plastic singular behaviors. The origin of their formation will be discussed at the end of the section.

Maps of the stress components σ_{11} (Fig. 6(c)–(e)) and σ_{22} (Fig. 6(f)–(h)) for the three different situations at $t=36.3$ h are presented in Fig. 6. For the elastic model, the σ_{11} component is nearly homogeneous through all the material with a value close to the applied stress σ_{11}^q . The homogeneity of σ_{11} is nothing but the consequence of mechanical equilibrium in a microstructure whose interfaces are perpendicular to the [100] direction. The only small heterogeneities of the σ_{11} field are in the horizontal channels where the value of σ_{11} is much smaller. Since the horizontal channels accommodate the misfit between the two phases ($\delta < 0 \rightarrow a_\gamma > a_\beta$) they are submitted to smaller local stresses. This point is also true in the viscoplastic simulations because, as detailed above, plastic activity is negligible in the horizontal γ channels. Their behavior can be considered as an elastic one. Contrary to the σ_{11} maps, the σ_{22} maps are very different in the three simulations. $|\sigma_{22}|$ has a much higher value in the elastic simulation. For both viscoplastic simulations, after a sufficient time, we observe a relaxation of the σ_{22} stress component (Fig. 6(f)–(h)) resulting from the plastic deformation of the γ channels. The behavior of σ_{33} (not shown) is qualitatively the same. These differences in σ_{22} and σ_{33} are the result of the previously described differences in the plastic field p and they explain the variations in kinetics observed between the three simulations in Fig. 5.

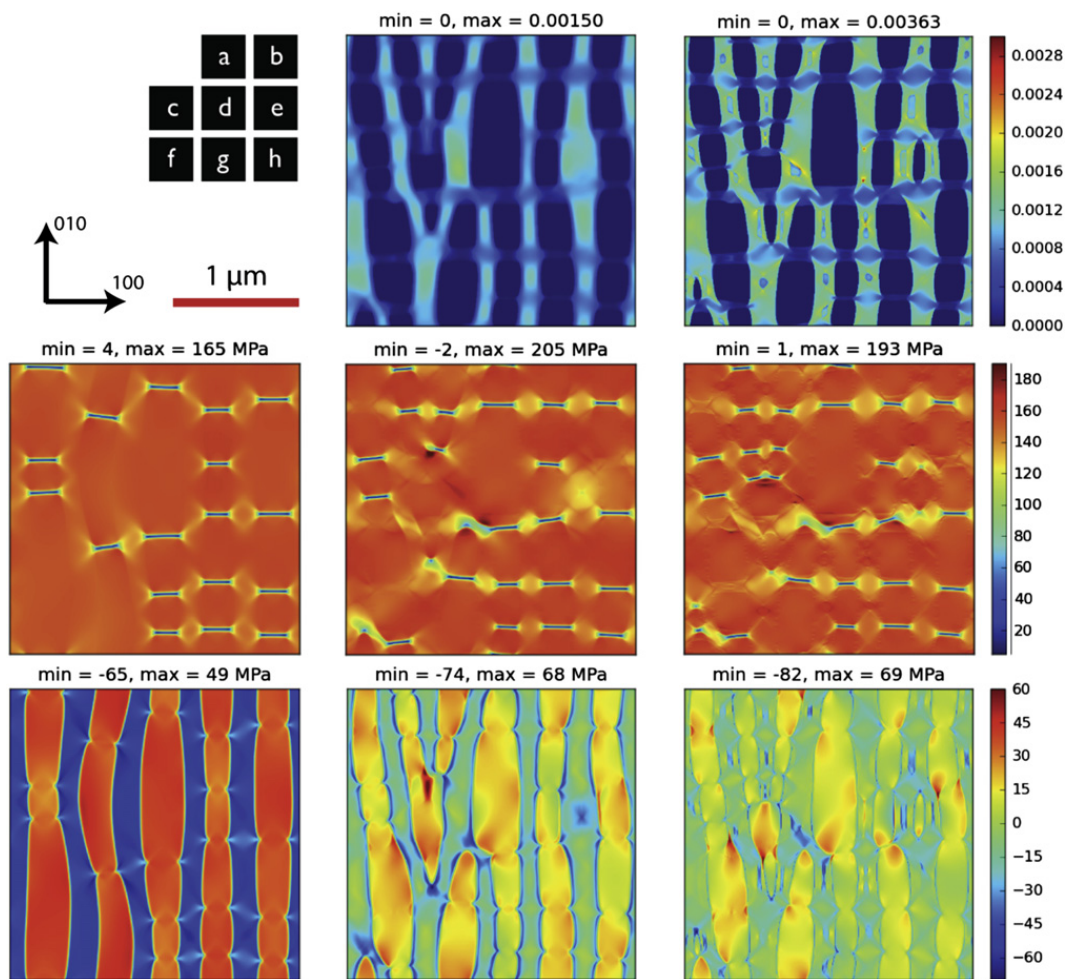


Fig. 6. Plastic and elastic fields obtained at $t=36.3$ h in the elastic model (first column), in the elasto-viscoplastic model including size effect (middle column) and in the elasto-viscoplastic model where $\tilde{\xi}=0$ (last column). The first row is the cumulative plastic strain field p and the second and third rows are the stress components σ_{11} and σ_{22} , respectively. The nomenclature of the images is indicated in the upper left corner.

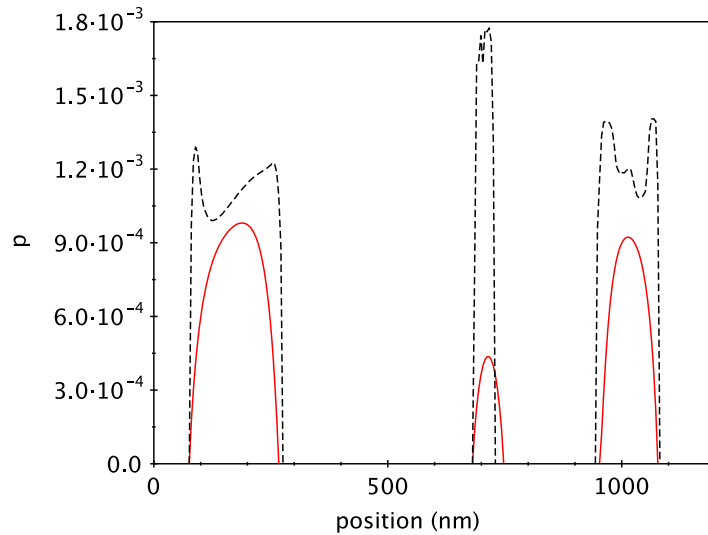


Fig. 7. Profiles of the cumulative plastic strain perpendicular to the rafts at $t=1$ h: $\tilde{\xi} = 0$ (dashed line); $\tilde{\xi} = 26$ nm (full red line). (For interpretation of the references to color in this figure caption, the reader is referred to the web version of this article.)

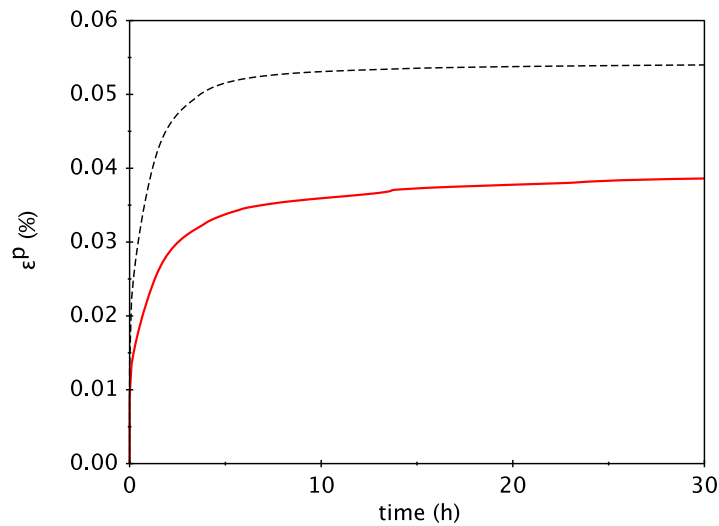


Fig. 8. Average plastic strain vs. time obtained from simulated creep experiment at $T = 950$ °C under 150 MPa: $\tilde{\xi} = 0$ (dashed line); $\tilde{\xi} = 26$ nm (full red line). (For interpretation of the references to color in this figure caption, the reader is referred to the web version of this article.)

In Fig. 8, the average plastic strain ε^p is plotted vs. time for the two viscoplastic cases. In both cases, a primary creep stage featuring a rapid increase of ε^p is observed when $t < 5$ h. At the end of this stage, a rafted microstructure can be observed (Fig. 5(e)–(h)). For $t > 5$ h, the evolution of ε^p becomes slow and almost linear. During this secondary creep stage, the microstructure remains stable in time (Fig. 5(g)–(j)). The time at which the secondary creep stage begins as well as the value of the plastic strain plateau are consistent with experiments on AM1 superalloys obtained in similar creep conditions (Diologent, 2002). As expected, introducing the size effect results in a strengthening of the material: ε^p is smaller with $\tilde{\xi} = 26$ nm (full red line) than with $\tilde{\xi} = 0$ (dashed line). The difference is more important during the primary creep stage when the microstructure still features a large distribution of γ channels widths. During the secondary creep stage, the microstructure exhibits well defined rafts. Plastic activity develops inside rather large vertical γ channels which are barely affected by the size effect. This explains the rather similar plastic behavior of the two viscoplastic models in the secondary creep stage.

During the creep experiment, a widening of the γ channels is observed leading to a decrease of the plastic size effects, in accordance with 1D calculations (Section 3.1.1). In addition, the kinematic hardening variable X evolves rapidly during the first stages of the experiment and reaches a plateau after 5 h in both simulations. The saturation value is found very close to the value $2C/3D$ expected in a 1D configuration. Note finally that after 5 h a slow evolution of both ε_{11}^p and X_{11} can still be observed for $\tilde{\xi} \neq 0$ but not for $\tilde{\xi} = 0$.

Note that in Fig. 8, there is no tertiary creep stage since the physical mechanisms responsible of the phenomenon are not included: the shearing of the γ' precipitates and the internal crack initiation resulting from porosity (MacLachlan et al., 2001).

Finally, we discuss the origin of the slight differences in plastic behavior which can be observed at the center of the γ channels. These regions are visible in Fig. 6(b) (also in Fig. 7) when $\tilde{\xi} = 0$ and subsist during microstructure evolution. The plastic strain inside these regions remains rather constant and the ulterior plasticity takes place around these areas. Note that the presence of these areas does not seem to impact significantly microstructure evolution, probably because they are not located close to the γ/γ' interfaces. These regions are not observed in experiments. These artifacts disappear when a plastic size effect, which regularizes the plastic rate, is operating.

4. Conclusion

An extension of a phase field model has been proposed, which captures microstructure evolutions coupled to viscoplasticity. In particular, the model accounts for the size effect of the plastic behavior beyond the volume fraction effect, i.e. for the hardening (resp. softening) induced by the decrease (resp. increase) of the size of the plastic regions. This effect may be rather important in heterogeneous materials because the size and the shape of the plastic regions evolve during thermo-mechanical treatments. To our knowledge, the plastic size effect had never been introduced in a phase field model using a continuous approach. The viscoplastic behavior is introduced at mesoscale using a strain gradient approach and is coupled to a phase field model within a thermodynamic consistent framework. The model has been applied to the microstructural evolution in Ni-base superalloys in creep conditions during which plasticity only proceeds inside the γ phase. The parameters of the model have been selected to mimic the behavior of the AM1 monocrystalline superalloy. We have assumed that plasticity in the γ channels can be described by continuum strain gradient viscoplasticity, in spite of their very small width. Several important physical phenomena, such as the ordered character of the γ' phase, the elastic inhomogeneity and anisotropy, the misfit, the hardening and the viscosity of the plasticity are included in the model.

Static configurations have first been used to emphasize the influence of the plastic size effect on the mechanical behavior of heterogeneous materials and to properly define the internal length scale of the plastic model. Then, 2D simulations have been performed to investigate the influence of the plastic size effect on the microstructural evolution during creep loading along a cubic axis. It has been found that plastic activity accelerates the formation of the rafts and leads to an almost frozen configuration of wavy rafts. Comparing the simulation results including or ignoring the plastic size effect, we have shown that, in these alloys, the size effect has only a moderate impact on the morphological evolution but is crucial to reproduce the macroscopic mechanical behavior of the material.

The model proposed in this paper will be extended to include plastic anisotropy and 3D simulations will be performed. In particular, in the context of Ni-base superalloys, this extension will open the possibility to investigate the microstructural evolution during creep experiments along complex loading axis.

Acknowledgments

The authors acknowledge the financial support of the French Agence Nationale de la Recherche (ANR) under reference ANR-BLAN08-1_321567 (project Couphin). The authors would like to thank Dr. A. Gaubert (Onera) for providing the SEM images.

Appendix A. Analytical solution of the model in 1D

In the case of a 1D configuration (Fig. 1 and Section 3.1.1) displacement reads

$$\begin{cases} u_1(x) = \bar{\varepsilon}_{11} x + u(x) \\ u_2(y) = \varepsilon_{22} y \\ u_3(z) = \varepsilon_{22} z \end{cases} \quad (22)$$

where $u(x)$ is the periodic fluctuation displacement and $\bar{\varepsilon}_{11}$ the average tensile strain field. Strain and stress tensors are

$$\tilde{\varepsilon} = \begin{pmatrix} \bar{\varepsilon}_{11} + u_{,1}(x) & 0 & 0 \\ 0 & \varepsilon_{22} & 0 \\ 0 & 0 & \varepsilon_{22} \end{pmatrix}, \quad \tilde{\sigma} = \begin{pmatrix} \sigma_{11} & 0 & 0 \\ 0 & \sigma_{22}(x) & 0 \\ 0 & 0 & \sigma_{22}(x) \end{pmatrix} \quad (23)$$

where $f_{,1}$ denotes the derivative of f with respect to the x coordinate. For this 1D geometry, coherency of the γ/γ' interface implies that ε_{22} is homogeneous. In addition, σ_{11} is also homogeneous to fulfill mechanical equilibrium. Under these conditions, the J_2 yield surface can be defined in stress space as

$$J_2(\tilde{\sigma}) = |\sigma_{11} - \sigma_{22}(x)| \quad (24)$$

Hooke's law holding in γ and γ' , we have

$$\begin{cases} \sigma_{11}'' = C_{11}[\bar{\varepsilon}_{11} + u_{,1}''(x)] + 2C_{12}\varepsilon_{22} \\ \sigma_{11}' = C_{11}[\bar{\varepsilon}_{11} + u_{,1}'(x) - p(x)] + 2C_{12}[\varepsilon_{22} + p(x)/2] \end{cases} \quad (25)$$

$$\begin{cases} \sigma_{22}^{\gamma\gamma}(x) = C_{12}[\bar{\varepsilon}_{11} + u_{,1}^{\gamma\gamma}(x)] + (C_{11} + C_{12})\varepsilon_{22} \\ \sigma_{22}^{\gamma}(x) = C_{12}[\bar{\varepsilon}_{11} + u_{,1}^{\gamma}(x) - p(x)] + (C_{11} + C_{12})[\varepsilon_{22} + p(x)/2] \end{cases} \quad (26)$$

Since σ_{11} is homogeneous, we get

$$\sigma_{11}^{\gamma} = \sigma_{11} = C_{11}[\bar{\varepsilon}_{11} + u_{,1}^{\gamma}(x) - p(x)] + 2C_{12}[\varepsilon_{22} + p(x)/2] = \text{Cst} \quad (27)$$

We consider a situation where the γ phase undergoes time independent plastic deformation. Using von Mises criterion, we get

$$R_0 + Hp(x) - A\Delta p(x) = |\sigma_{11} - \sigma_{22}^{\gamma}(x)| \quad (28)$$

Using Eq. (26) into Eq. (28) gives

$$\left[H + \frac{1}{2} \frac{E}{1-\nu} \right] p(x) - A\Delta p(x) = T - R_0 \quad (29)$$

where $E/(1-\nu) = (C_{11}-C_{12})(C_{11}+2C_{12})/C_{11}$ and $T = (C_{11}-C_{12})/C_{11}[\sigma_{11} - (C_{11}+2C_{12})\varepsilon_{22}]$.

Eq. (29) is a second order differential equation. Integrating this equation leads to

$$p(x) = \mathcal{M} \left(1 - \frac{\cosh(\omega x)}{\cosh(\omega s/2)} \right) \quad (30)$$

where

$$\omega^2 = \frac{H + \frac{1}{2} \frac{E}{1-\nu}}{A} \quad \text{and} \quad \mathcal{M} = \frac{T - R_0}{H + \frac{1}{2} \frac{E}{1-\nu}}$$

The two unknown constants σ_{11} and ε_{22} are determined using the following boundaries conditions $\langle \sigma_{11} \rangle = \sigma_{11}$ and $\langle \sigma_{22} \rangle = 0$. We obtain

$$\begin{cases} \sigma_{11} = (C_{11} + 2C_{12})(\bar{\varepsilon}_{11} + 2\varepsilon_{22}) \\ \varepsilon_{22} = \frac{B}{B_{1-\nu} - (C_{11} + C_{12})} R_0 - \frac{B_{1-\nu} - C_{12}}{B_{1-\nu} - (C_{11} + C_{12})} \bar{\varepsilon}_{11} \end{cases} \quad (31)$$

where

$$B = \frac{(C_{12} - C_{11})}{2(\ell + s)(H + \frac{1}{2} \frac{E}{1-\nu})} \left[s - \frac{2}{\omega} \tanh(\omega s/2) \right]$$

The continuity of plastic strain $p(x)$ and the continuity of displacement at the interface $x_1 = s/2$ can be used to determine the heterogeneous displacement field $u(x)$.

References

- Aifantis, E.C., 1987. The physics of plastic deformation. *Int. J. Plasticity* 3, 211.
- Ammar, K., Appolaire, B., Cailletaud, G., Forest, S., 2009. Combining phase field approach and homogenization methods for modelling phase transformation in elastoplastic media. *Eur. J. Comput. Mech.* 18, 485.
- Ammar, K., Appolaire, B., Cailletaud, G., Forest, S., 2011. Phase field modeling of elasto-plastic deformation induced by diffusion controlled growth of a misfitting spherical precipitate. *Philos. Mag. Lett.* 91, 164.
- Anand, L., Gurtin, M.E., Fried, E., 2010. *The Mechanics and Thermodynamics of Continua*. Cambridge University Press.
- Ashby, M.F., 1971. The deformation of plastically non-homogeneous alloys. In: *Strengthening Methods in Crystals*. Applied Science Publishers, London.
- Boisse, J., Lecoq, N., Patte, R., Zapolsky, H., 2007. Phase-field simulation of coarsening of γ precipitates in an ordered γ' matrix. *Acta Mater.* 55, 6151.
- Boussinot, G., Finel, A., Le Bouar, Y., 2009. Phase-field modeling of bimodal microstructures in nickel-based superalloys. *Acta Mater.* 57, 921.
- Boussinot, G., Le Bouar, Y., Finel, A., 2010. Phase-field simulations with inhomogeneous elasticity: comparison with an atomic-scale method and application to superalloys. *Acta Mater.* 58, 4170.
- Cordero, N., Gaubert, A., Forest, S., Busso, E., Gallerneau, F., Kruch, S., 2010. Size effects in generalised continuum crystal plasticity for two-phase laminates. *J. Mech. Phys. Solids* 58, 1963.
- Diologent, F., 2002. *Comportement en fluage et en traction de superalliages monocristallins à base de nickel*. Ph.D. Thesis, Université Paris XI-Orsay.
- Diologent, F., Caron, P., d'Almeida, T., Jacques, A., Bastie, P., 2003. The γ - γ' mismatch in Ni based superalloys: in situ measurements during a creep test. *Nucl. Instrum. Meth. B* 200, 346.
- Eringen, A.C., Suhubi, E.S., 1964. Nonlinear theory of simple micro-elastic solids. *Int. J. Eng. Sci.* 2, 189.
- Espié, L., 1996. *Etude expérimentale et modélisation numérique du comportement de monocristaux de superalliages*. Ph.D. Thesis, ENSMP.
- Fahrman, M., Hermann, W., Fahrman, E., Boegli, A., Pollock, T.M., Sockel, H.G., 1999. Determination of matrix and precipitate elastic constants in γ - γ' Ni-base model alloys, and their relevance to rafting. *Mater. Sci. Eng. A* 260, 212.
- Finel, A., Le Bouar, Y., Gaubert, A., Salman, U., 2010. Phase field methods: microstructures, mechanical properties and complexity. *C.R. Physique* 11, 245.
- Fleck, N.A., Hutchinson, J.W., 1997. Strain gradient plasticity. *Adv. Appl. Mech.* 33, 295.
- Forest, S., Aifantis, E.C., 2010. Some links between recent gradient thermo-elasto-plasticity theories and the thermomechanics of generalized continua. *Int. J. Solids Struct.* 47, 3367.
- Forest, S., Cailletaud, G., Sievert, R., 1997. A cosserat theory for elastoviscoplastic single crystals at finite deformation. *Arch. Mech.* 49, 705.
- Forest, S., Sievert, R., 2003. Elastoviscoplastic constitutive frameworks for generalized continua. *Acta Mech.* 160, 71.
- Fujiwara, F., Watanabe, M., Nemoto, Z.H.N., Noumi, K., Simozaki, T., 1999. International Conference on Solid-Solid Transformations (JIMIC-3).
- Ganghoffer, J., Denis, S., Gautier, E., Sjöström, S., 1997. Micromechanical analysis of the finite element calculation of a diffusional transformation. *J. Mater. Sci.* 32, 4941.

- Ganghoffer, J., Simonsson, K., Denis, S., Gautier, E., Sjöström, S., Simon, A., 1994. Martensitic transformation plasticity simulations by finite elements. *J. Phys. IV* 04, C3–C215.
- Gaubert, A., Finel, A., Le Bouar, Y., Boussinot, G., 2008. Viscoplastic phase field modelling of rafting in Ni base superalloys. In: Jeulin, D., Forest, S. (Eds.), *Continuum Models and Discrete Systems CMDS11*, Mines Paris Les Presses, pp. 161.
- Gaubert, A., 2009. Modélisation des effets de l'évolution microstructurale sur le comportement mécanique du superalliage monocristallin AM1. Ph.D. Thesis, Mines ParisTech.
- Gaubert, A., Le Bouar, Y., Finel, A., 2010. Coupling phase field and viscoplasticity to study rafting in Ni-based superalloys. *Philos. Mag. B* 90, 375.
- Guo, X.H., Shi, S.Q., 2005. Elastoplastic phase field model for microstructure evolution. *Appl. Phys. Lett.* 87, 221910.
- Gurtin, M., Anand, L., 2009. Thermodynamics applied to gradient theories involving the accumulated plastic strain: the theories of Aifantis and Fleck & Hutchinson and their generalization. *J. Mech. Phys. Solids* 57, 405.
- Gurtin, M.E., 2002. A gradient theory of single-crystal viscoplasticity that accounts for geometrically necessary dislocations. *J. Mech. Phys. Solids* 50, 5.
- Hall, E., 1951. The deformation and aging of mild steel. Part iii: discussion and results. *Proc. Phys. Soc. London* 64, 747.
- Hanriot, F., 1993. Comportement du superalliage monocristallin AM1 sous sollicitations cycliques. Ph.D. Thesis, ENSMP.
- Hu, S.Y., Chen, L.Q., 2001. A phase field model for evolving microstructures with strong elastic inhomogeneity. *Acta Mater.* 49, 1879.
- Khachaturyan, A.G., 1983. *The Theory of Structural Transformations in Solids*. Wiley, New York.
- Koslowski, M., Cuitino, A.M., Ortiz, M., 2002. A phase-field theory of dislocation dynamics, strain hardening and hysteresis in ductile single crystals. *J. Mech. Phys. Solids* 50, 2597.
- Le Bouar, Y., Loiseau, A., Khachaturyan, A.G., 1998. Origin of chessboard-like structures in decomposing alloys. Theoretical model and computer simulation. *Acta Mater.* 46, 2777.
- Lemaitre, J., Chaboche, J.L., 1990. *Mechanics of Solid Materials*. Cambridge University Press.
- Levkovitch, V., Sievert, R., Svendsen, B., 2006. Simulation of deformation and lifetime behavior of a fcc single crystal superalloy at high temperature under low-cycle fatigue loading. *Int. J. Fatigue* 28, 1791.
- Li, D.F., Zhang, X.M., Gautier, E., Zhang, J.S., 1998. Morphology transitions of deformation-induced thin-plate martensite in Fe–Ni–C alloys. *Acta Mater.* 46, 4827.
- MacLachlan, D.W., Wright, L.W., Gunturi, S., Knowles, D.M., 2001. Constitutive modelling of anisotropic creep deformation in single crystal blade alloys SRR99 and CMSX-4. *Int. J. Plasticity* 17, 441.
- Mindlin, R.D., Eshel, N.N., 1968. On first strain-gradient theories in linear elasticity. *Int. J. Solids Struct.* 4, 109.
- Onuki, A., Nishimori, H., 1991. Anomalously slow domain growth due to a modulus inhomogeneity in phase separating alloys. *Phys. Rev. B* 43, 13649.
- Rodney, D., Finel, A., 2001. Phase field methods and dislocations. In: Aindow, M., Asta, M., Glazov, M., Medlin, D., Rollet, A., Zaiser, M. (Eds.), *Influences of Interface and Dislocation Behavior on Microstructure Evolution*. MRS Proceedings vol. 652.
- Rodney, D., Le Bouar, Y., Finel, A., 2003. Phase field methods and dislocations. *Acta Mater.* 51, 17.
- Royer, A., Bastie, P., Véron, M., 1998. In situ determination of γ' phase volume fraction and of relations between lattice parameters and precipitate morphology in Ni-based single crystal superalloy. *Acta Mater.* 46, 5357.
- Sieborger, D., Knake, H., Glatzel, U., 2001. Temperature dependence of the elastic moduli of the nickel-base superalloy cmsx-4 and its isolated phases. *Mater. Sci. Eng. A* 298, 26.
- Steinmann, P., 1996. Views on multiplicative elastoplasticity and the continuum theory of dislocations. *Int. J. Eng. Sci.* 34, 1717.
- Su, T.J., Aebly-Gautier, E., Denis, S., 2006. Morphology changes in bainite formed under stress. *Scripta Mater.* 54, 2185.
- Svendsen, B., 2002. Continuum thermodynamic models for crystal plasticity including the effects of geometrically-necessary dislocations. *J. Mech. Phys. Solids* 50, 1297.
- Thuinet, L., Legris, A., 2010. Elastically driven morphology of coherent trigonal precipitates inside a close-packed hexagonal matrix. *Acta Mater.* 58, 2250.
- Ubachs, R.L.J.M., Schreurs, P.J.G., Geers, M.G.D., 2005. Phase field dependent viscoplastic behaviour of solder alloys. *Int. J. Solids Struct.* 42, 2533.
- Uehara, T., Tsujino, T., Ohno, N., 2007. Elasto-plastic simulation of stress evolution during grain growth using a phase field model. *J. Cryst. Growth* 300, 530.
- Viardin, A., 2010. Modélisation par champ de phases de la croissance de la ferrite allotriomorphe dans les aciers Fe–C–Mn. Ph.D. Thesis, INPL.
- Wang, Y., Banerjee, D., Su, C.C., Khachaturyan, A.G., 1998. Field kinetic model and computer simulation of precipitation of L1₂ ordered intermetallics from f.c.c. solid solution. *Acta Mater.* 46, 2983.
- Wang, Y.U., Jin, Y.M., Cuitino, A.M., Khachaturyan, A.G., 2001. Nanoscale phase field microelasticity theory of dislocations: model and 3d simulations. *Acta Mater.* 49, 1847.
- Wang, Y.U., Jin, Y.M., Khachaturyan, A.G., 2004. The effects of free surfaces on martensite microstructures: 3d phase field microelasticity simulation study. *Acta Mater.* 52, 1039.
- Wen, H., Denis, S., Gautier, E., 1996. Computer simulation of martensitic transformation under stress. *J. Phys. IV* 06, C1–C475.
- Yamanaka, A., Takaki, T., Tomita, Y., 2008. Elastoplastic phase-field simulation of self- and plastic accommodations in cubic \rightarrow tetragonal martensitic transformation. *Mater. Sci. Eng. A* 491, 378.
- Yang, J.X., Zheng, Q., Sun, X.F., Guan, H.R., Hu, Z.Q., 2007. Morphological evolution of γ' phase in k465 superalloy during prolonged aging. *Mater. Sci. Eng. A* 457, 148.
- Zhou, N., Shen, C., Mills, M., Wang, Y., 2008. Contributions from elastic inhomogeneity and from plasticity to γ' rafting in single-crystal Ni–Al. *Acta Mater.* 56, 6156.
- Zhou, N., Shen, C., Mills, M., Wang, Y., 2010. Large-scale three-dimensional phase field simulation of γ' rafting and creep deformation. *Philos. Mag. B* 90, 405.